Author/s:
Wang, Z;Gao, J;Zhou, J;Gong, J;Shang, L;Ye, H;He, F;Peng, S;Lin, Z;Li, Y;Caruso, F

Title:
Engineering Metal–Phenolic Networks for Solar Desalination with Directional Salt Crystallization

Date:
2023-01-05

Citation:
Wang, Z., Gao, J., Zhou, J., Gong, J., Shang, L., Ye, H., He, F., Peng, S., Lin, Z., Li, Y. & Caruso, F. (2023). Engineering Metal–Phenolic Networks for Solar Desalination with Directional Salt Crystallization. Advanced Materials, 35 (1), https://doi.org/10.1002/adma.202209015.

Persistent Link:
https://hdl.handle.net/11343/325332

ADVANCED MATERIALS
www.advmat.de

Engineering Metal–Phenolic Networks for Solar Desalination with Directional Salt Crystallization

Zhenxing Wang, Jie Gao, Jiajing Zhou, Jingwen Gong, Longwen Shang, Haobin Ye, Fang He, Shaoqin Peng, Zhixing Lin, Yuexiang Li,* and Frank Caruso**

Solar desalination is one of the most promising strategies to address the global freshwater shortage crisis. However, the residual salt accumulated on the top surface of solar evaporators severely reduces light absorption and steam evaporation efficiency, thus impeding the further industrialization of this technology. Herein, a metal–phenolic network (MPN)-engineered 3D evaporator composed of photothermal superhydrophilic/superhydrophobic sponges and side-twining hydrophilic threads for efficient desalination with directional salt crystallization and zero liquid discharge is reported. The MPN coatings afford the engineering of alternating photothermal superhydrophilic/superhydrophobic sponges with high heating efficiency and defined vapor escape channels, while the side-twining threads induce site-selective salt crystallization. The 3D evaporator exhibits a high and stable indoor desalination rate (≈2.3 kg m^{-2} h^{-1}) of concentrated seawater (20 wt%) under simulated sun irradiation for over 21 days without the need for salt crystallization inhibitors. This direct desalination is also achieved in outdoor field operations with a production rate of clean water up to ≈1.82 kg m^{-2} h^{-1} from concentrated seawater (10 wt%). Together with the high affinity and multiple functions of MPNs, this work is expected to facilitate the rational design of solar desalination devices and boost the research translation of MPN materials in broader applications.

1. Introduction

Freshwater shortage has become a major world concern owing to the large proportion of water on earth being saline and expansion of the world population.[1–4] Accordingly, thermal distillation (e.g., multistage flash distillation) and membrane-based technologies (e.g., reverse osmosis) have been developed for seawater desalination but these technologies are often energy-intensive and rely on non-renewable energy resources (e.g., fossil fuels).[5–7] Moreover, the energy input requirement for reverse osmosis increases considerably with the increasing concentration of salts in brine during the filtration process.[8] Consequently, the remaining highly concentrated waste brine (>7 wt%) is typically discharged to adjacent water bodies (e.g., rivers), thus causing hazards to the aquatic ecosystem.[9] Recently, solar-driven interfacial evaporation desalination has attracted increasing attention owing to the clean and abundant solar energy available naturally and its higher efficiency by localizing heat at the air–water interface rather than heating bulk water as performed in traditional solar evaporators.[10–12] However, the rapidly generated steam at the interface causes precipitated salt to accumulate on the top surface of the evaporators, which not only hinders heat conversion from sunlight but also blocks interior channels for water flux and escape of vapor, leading to a significant decrease in the efficiency and lifetime of the solar evaporators.[13–16]

Several strategies have been explored to regulate salt mitigation inside evaporators, among which creating a Janus bilayer structure (i.e., a bottom hydrophilic layer for water pumping and an upper hydrophobic layer for solar absorption) is one of the most promising strategies.[17–21] In this approach, salts are exclusively deposited within the hydrophilic layers rather than on the top surface of superhydrophobic photothermal materials designed to absorb solar energy. However, most superhydrophobic modification strategies require toxic solvents or adhesives, and such superhydrophobic photothermal coatings suffer from relatively poor affinity to substrates (i.e., detachment) in underwater environments, especially under a high water flush pressure.[22–24] Therefore, designing an all-in-one evaporator via a simple preparation process that can exhibit robust

Z. Wang, J. Gao, J. Gong, L. Shang, H. Ye, F. He, S. Peng, Y. Li
College of Chemistry
Nanchang University
Nanchang 330031, P. R. China
E-mail: liyx@ncu.edu.cn
J. Zhou
Department of NanoEngineering
University of California
9500 Gilman Drive, La Jolla, San Diego, CA 92093, USA
Z. Lin, F. Caruso
Department of Chemical Engineering
The University of Melbourne
Parkville, Victoria 3010, Australia
E-mail: zhixing.lin@unimelb.edu.au; fcaruso@unimelb.edu.au
The ORCID identification number(s) for the author(s) of this article can be found under https://doi.org/10.1002/adma.202209015.

DOI: 10.1002/adma.202209015

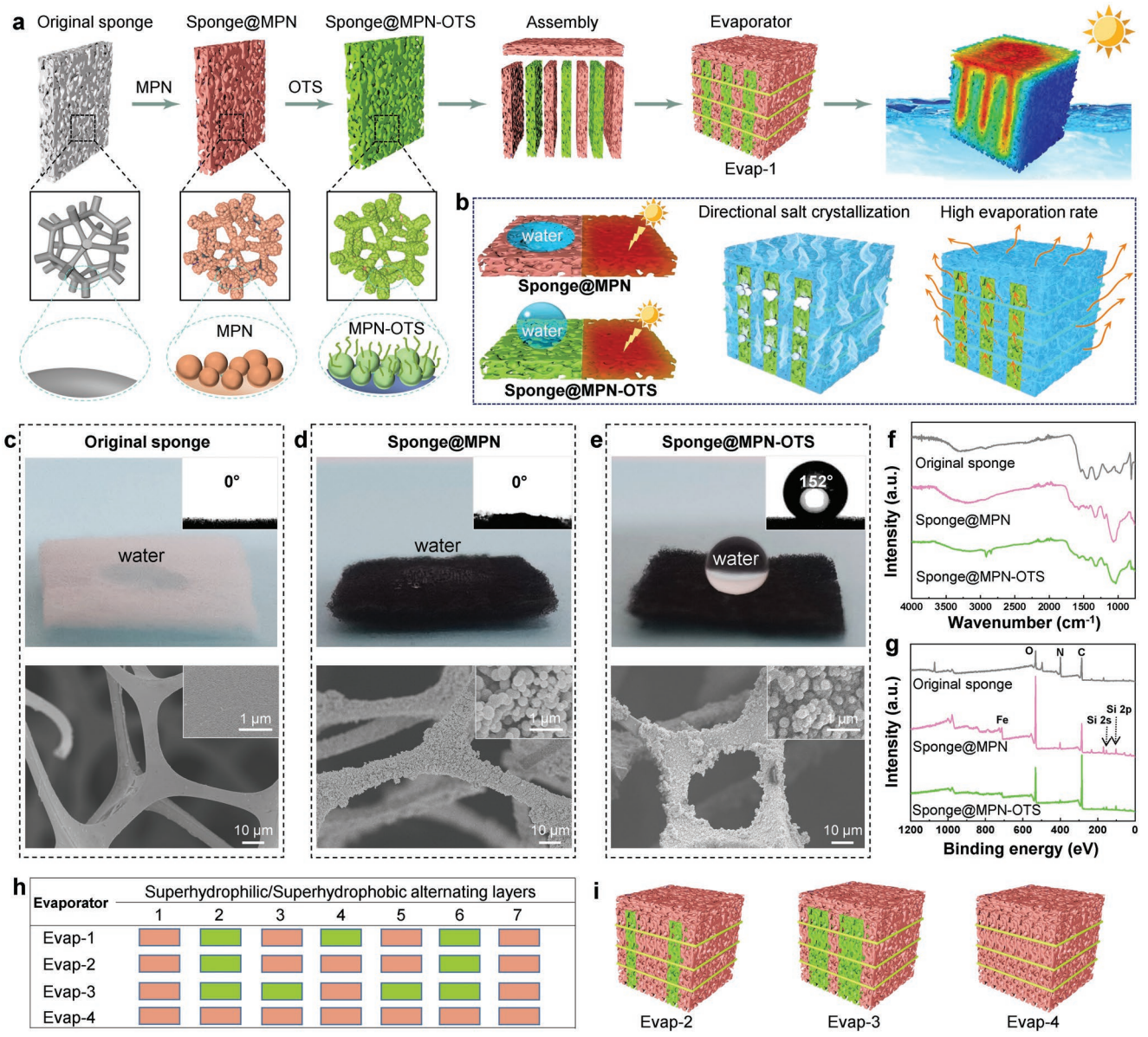

Figure 1. a) Schematic of the modification of sponges by MPNs and their assembly into 3D evaporators for solar desalination. b) Schematic of the MPN-engineered sponges with photothermal and selective wettability properties, which enable directional salt crystallization and high evaporation rates within the 3D evaporator. c–e) Photographs and SEM images of original sponge (c), sponge@MPN (d), and sponge@MPN-OTS (e). f) ATR-FTIR and g) XPS spectra of original and MPN-modified sponges. h) Schematic summary of the composition and arrangement of sponges in different evaporators. i) Schematic illustration of Evap-2, Evap-3, and Evap-4.

photothermal coating layers, a high evaporation rate, high salt mitigation ability, and a low environmental impact is challenging but imperative.

Metal–phenolic networks (MPNs) have recently attracted widespread interest owing to their porous structure and strong affinity to various substrates.[25–28] The flexible combination of metal ions and abundant availability of natural phenolic ligands enables the engineering of MPNs with a wide range and tunable physicochemical properties, including photothermal and selective wettability, which are desirable for solar desalination applications.[29–32] Herein, we report a strategy, combining materials design and structural engineering, to prepare a 3D solar evaporator for highly efficient, long-term, and sustained desalination of high-salinity brine (**Figure 1**a). Specifically, sponges were first modified with superhydrophilic MPNs exhibiting photothermal effects. The resulting sponge-modified MPNs were then selectively engineered as superhydrophobic interfacial layers via catechol/gallol groups.[27,31] The 3D evaporator was constructed by alternating and horizontally stacking the superhydrophilic and superhydrophobic sponges, which were then tied with hydrophilic nylon threads. A superhydrophilic sponge was used as the top cover, sitting perpendicular on top of the stacked sponges. The multiple interlaced superhydrophobic photothermal sponges not only can provide abundant vapor

escape channels but also can generate heat to accelerate the evaporation of water in the bilateral superhydrophilic sponges (Figure 1b). Notably, the addition of the side-twining hydrophilic threads can effectively induce directional salt crystallization, thus avoiding salt accumulation on the top surface of the evaporator and achieve zero liquid discharge.[33] Therefore, additional salt inhibitors, which are often used in other evaporators and may cause issues for the subsequent recycling and purification of the salt, are not required in our current approach.[34] The 3D evaporator exhibited excellent indoor performance with a very high and stable evaporation rate (≈2.3 kg m^{-2} h^{-1}) for the 21-day period examined in the presence of highly concentrated brine (20 wt%), which is among the best performance reported in the literature. The 3D evaporator also possessed a stable and highly efficient water production rate of ≈1.82 kg m^{-2} h^{-1} for concentrated seawater (10 wt%) during the outdoor field operation process. Our study not only expands the potential applications of MPN-based materials but also underpins the structural engineering for the rational design of solar evaporators.

2. Results and Discussion

2.1. Fabrication of MPN-Engineered Sponges and 3D Evaporators

Melamine sponges were chosen as the substrates as they are commercially available and have high porosity to generate the capillary forces required for pumping water (Figure 1c, pore size: ≈100 μm).[35] The melamine sponges were engineered with modified MPNs with selective wettability to achieve photothermal and superhydrophilic/superhydrophobic properties. Briefly, the sponge was incubated with tannic acid (TA) and (3-aminopropyl)triethoxysilane (APTES), and Fe^{3+} ions were then added to cross-link the TA–APTES complexes by metal coordination (Figure S1, Supporting Information). The sponge changed from white to black upon formation of the MPN coating. The introduction of APTES partially cross-linked the polyphenol and therefore increased the stability of the coatings. The coated sponge was superhydrophilic owing to the abundant hydrophilic groups derived from TA (Figure 1d; Figure S2 and S3, Supporting Information). The superhydrophilic (modified) sponge (i.e., sponge@MPN) exhibited photothermal properties that originated from the high photothermal conversion efficiency of the black Fe^{3+}–TA MPNs.[36] The sponge@MPN was further conjugated with octadecyltrimethoxysilane (OTS) to form the superhydrophobic sponge (sponge@MPN-OTS) while maintaining the photothermal properties (Figure 1a; Figure S4, Supporting Information). The superhydrophobicity was ascribed to the micro-nano structures and the hydrophobic alkyl chains (Figure 1e; Figure S5, Supporting Information). The formation of superhydrophilic and superhydrophobic MPN coatings was further confirmed by the presence of the characteristic peaks (1600–1450 cm^{-1}) of TA from the attenuated-total-reflectance Fourier transform infrared (ATR-FTIR) spectroscopy analysis and Fe signal from the X-ray photoelectron spectroscopy (XPS) analysis (Figure 1f,g; Figure S3 and Table S1, Supporting Information). This MPN-mediated strategy can be applied to various substrates (e.g., polyvinylidene fluoride, nylon fabric, filter paper, and wood) and to endow them with selective wettability and photothermal properties (Figure S6–S8, Supporting Information).

Four types of 3D evaporators with the same exterior dimensions (1 cm × 1 cm × 1.14 cm) were fabricated by varying sponge composition and permutation to establish the material design and structural engineering requirements for achieving high-performance solar evaporators (Figure 1h; Figure S9, Supporting Information). For example, the first evaporator (Evap-1) was constructed from the horizontal arrangement of four sponge@MPN and three sponge@MPN-OTS, fixed by three hydrophilic threads running across the stacked sponges, and a sponge@MPN placed perpendicular on top of the stacked layers (Figure 1a; Figure S9, Supporting Information). The hydrophilic threads were used to induce salt crystallization and the hydrophilic sponge, forming the top surface of the evaporator, was used to maximize the evaporation area of water vapor. Three other evaporators were constructed similarly but with different permutations and combinations of the stacked superhydrophilic and superhydrophobic sponges (Figure 1h,i; Figure S9, Supporting Information).

2.2. Selective Water Transportation and Photothermal Effects

Selective water transportation is essential for the rational design of solar evaporators. Thus, the water-pumping channels and flow rate in the modified sponges and evaporators were first investigated. Water rapidly diffused into sponge@MPN and was efficiently transported upward when highly bent with a speed up to 8.4 mm s^{-1} (**Figure 2**a; Figure S10, Movies S1 and S2, Supporting Information). The efficient pumping ability of sponge@MPN is driven by capillary forces owing to its highly porous structure and superhydrophilic nature. In contrast, an air cushion was observed around sponge@MPN-OTS in water, indicating that water could not diffuse into the superhydrophobic sponge. The selective water-pumping channels were further validated within the 3D evaporators using a water supply device (Figure S11, Supporting Information). To visualize water flow in Evap-1, a white hydrophilic thread was wrapped around the surface of each sponge and the solution was dyed red. All white threads attached to the superhydrophilic sponge@MPN became red within seconds, while the threads on sponge@MPN-OTS remained white even after extended exposure to the solution for 24 h (Figure 2b; Figure S12, Supporting Information), confirming the presence of selective water-pumping channels inside the evaporators. The existence of water-repelling channels, operating as gas escape channels (Figure S13, Supporting Information), inside evaporators is essential for facilitating the rapid diffusion of the generated water steam into the atmosphere. The use of the hydrophilic sponge on the top of the alternately arranged superhydrophilic and superhydrophobic sponges (e.g., Evap-1) prevented the direct contact of the superhydrophobic photothermal layers with air and related potential heat loss (Figure 2c,d). The water flow and distribution in Evap-1 were further confirmed by using a fluorescent aqueous solution, which avoided the use of threads (Figure 2e).

Solar energy absorption and related light-to-thermal conversion efficiency are essential properties that dictate the

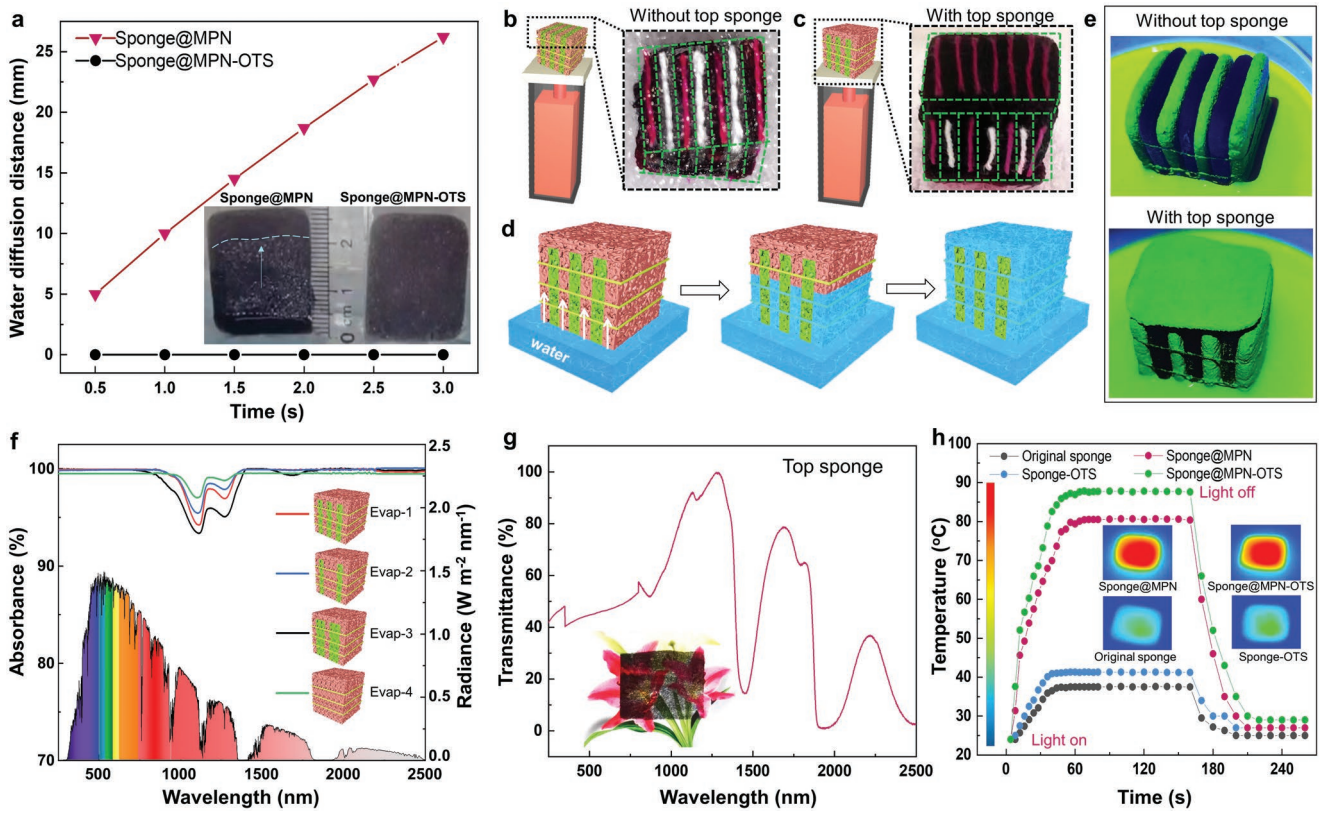

Figure 2. a) Upward distance traveled by water as a function of time within different sponges. The insets are photographs of sponge@MPN and sponge@MPN-OTS after immersion in water. b,c) Schematic and photographs of Evap-1 without (b) or with (c) top sponge cover after contacting with dyed water. d) Schematic of the diffusion process of water within the evaporators. e) Photographs of the immersion of Evap-1 with or without a top sponge cover in fluorescent aqueous solution under UV light. f,g) UV–vis absorption spectra of different evaporators (f) and top sponge cover (g). h) Thermal infrared images of different sponges in the presence or absence of solar irradiation in air.

performance of evaporators. The light absorption properties of the four evaporators containing water in their pores was characterized by UV–vis spectroscopy (Figure 2f). As the top sponge@MPN displayed a relatively high transmittance (Figure 2g), the light absorption ability of the evaporators could be mainly ascribed to the water content in the stacked sponges. All evaporators absorbed more than 95% of the input energy (Table S2, Supporting Information), with Evap-4 exhibiting the highest light absorption efficiency (i.e., 98%). This slightly higher light absorption efficiency displayed by Evap-4 is ascribed to the higher volume of water inside Evap-4 (compared with that in the other evaporators) as water can reduce light reflectance.[37] The light-to-thermal conversion of the sponges was subsequently investigated. As observed in Figure 2h, the surface temperatures of sponge@MPN (≈80 °C) and sponge@MPN-OTS (≈90 °C) were significantly higher than those of the original sponge (≈37 °C) and sponge-OTS (≈41 °C) owing to the photothermal effects endowed by the MPNs in the modified sponges. Interestingly, the superhydrophobic modification by conjugating with OTS, either with or without MPN intermediate coatings, slightly increased the surface temperature of the sponges, indicating that surface wettability also contributed to the photothermal effects of the sponges.

2.3. Indoor Solar Desalination and Directional Salt Crystallization

The solar-driven water evaporation performance of the different evaporators was then evaluated in a pure water system (Figure S14, Supporting Information). As shown in **Figure 3**a, the water evaporation rates of Evap-1, Evap-2, Evap-3, and Evap-4 were 2.84, 2.68, 2.51, and 2.39 kg m^{-2} h^{-1}, respectively, which were significantly higher than that of pure water in the absence of an evaporator (0.47 kg m^{-2} h^{-1}). Considering the similar light exposure area and absorption efficiency for all four evaporators, the evaporation rate was likely dependent on the different evaporation surface areas within the evaporators. Specifically, the superhydrophobic sponge@MPN-OTS is expected to increase the water evaporation area by creating an interfacial water vapor escape channel (Figure 3b). Therefore, the evaporation area was calculated based on the water-air interface areas of the water-filled superhydrophilic sponges (i.e., the interface between sponge@MPN to air and sponge@MPN to sponge@MPN-OTS). The water evaporation areas determined for Evap-1, Evap-2, Evap-3, and Evap-4 were ≈10.6, ≈8.5, ≈8.2, and 5 cm^2, respectively (Figure 3c), which accords with the trend of evaporation rate observed for the evaporators.

Notably, the high water evaporation rate of Evap-1 is also related to the photothermal sponge@MPN-OTS, which can

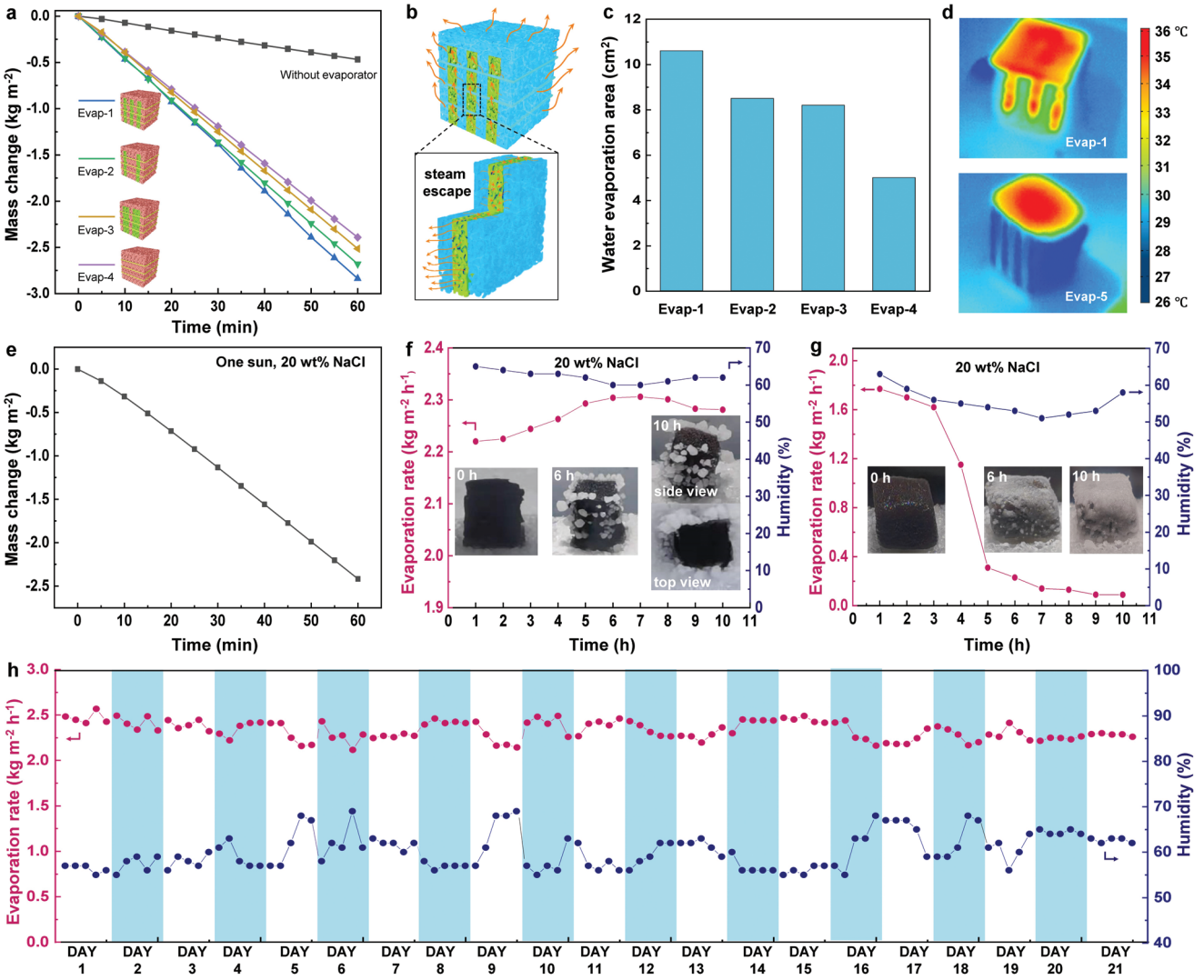

Figure 3. a) Changes in the amount of water evaporated as a function of time using 3D evaporators. b) Schematic of the multiple gas escape channels within Evap-1. c) Potential surface areas for water evaporation within different 3D evaporators. d) Thermal infrared images of Evap-1 and Evap-5 (both infiltrated with water) after irradiation for 15 min under one sun. e) Changes in the amount of water evaporated as a function of time during treatment of 20 wt% brine using 3D evaporators. f,g) Evaporation rates of water during treatment of 20 wt% brine using Evap-1 (f) or Evap-5 (g). The insets are photographs of the related evaporators with salt crystals formed at different treatment times. h) Stability of the evaporation rate of Evap-1 during treatment of 20 wt% seawater.

generate a higher temperature at the air–water interface to accelerate the evaporation of water. To confirm this, Evap-5 with the same structure and size as Evap-1 was prepared, except that the superhydrophobic sponge was replaced with sponge-OTS (Figures S15–S17, Supporting Information). The evaporators were kept running above a water chamber under one sun irradiation for 15 min to obtain the steady-state temperature and then characterized by thermal infrared imaging. As shown in Figure 3d, the temperature of sponge@MPN-OTS (≈35 °C) within Evap-1 was significantly higher than that of sponge-OTS (≈29 °C) within Evap-5. The higher temperature of sponge@MPN-OTS can consequently more effectively heat the adjacent sponge@MPN, leading to a higher water evaporation rate in Evap-1 than that in Evap-5 (Figure S18, Supporting Information). Evap-1 was chosen as a model for the subsequent studies due to its highest performance displayed among all evaporators in the pure water system.

We next investigated the solar desalination and anti-salt-fouling performance of Evap-1 and Evap-5 for high-salinity brine (e.g., 20 wt%). When treating 20 wt% NaCl solution under one sun irradiation (1 kW m^{-2}, 28 °C, relative humidity 60%), the water evaporation rate of Evap-1 reached up to ≈2.3 kg m^{-2} h^{-1} (Figure 3e), which is among the best performance reported in the literature (Figure S19, Supporting Information). The performance of the evaporators was further evaluated under simulated continuous operation for 10 h per day with a total solar irradiation of 10 kW m^{-2}, which is higher than the operation requirement of the US annual average daily solar irradiation (≈4.5 kW m^{-2}).[38] Evap-1 exhibited an overall stable water evaporation rate with slight fluctuations (2.2–2.3 kg m^{-2} h^{-1}), which

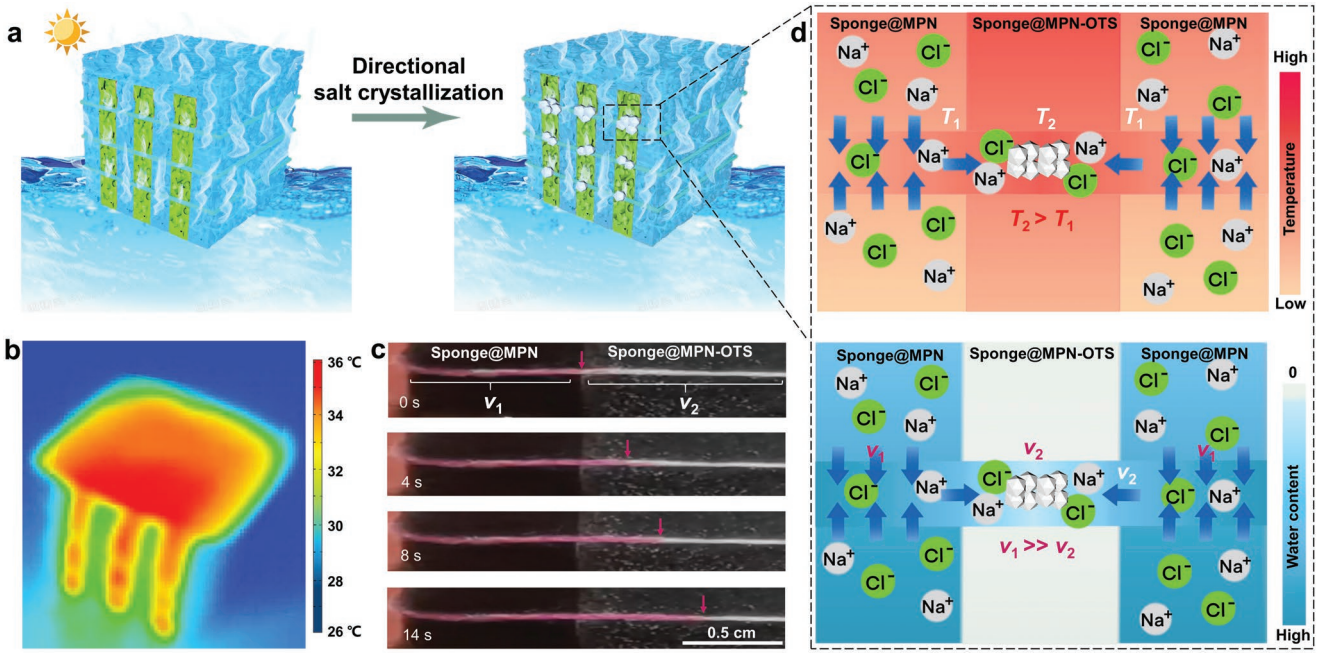

Figure 4. a) Schematic of directional salt crystallization within 3D evaporators. b) Thermal infrared image of the temperature distribution of sponge@MPN and sponge@MPN-OTS within Evap-1. c) Photograph of water flow rate, V_1 and V_2, on the thread that contacts sponge@MPN and sponge@MPN-OTS, respectively, within Evap-1. d) Schematic of the temperature distribution and water flow rate in the thread, sponge@MPN, and sponge@MPN-OTS.

may be mainly attributed to changes in the relative humidity (60–65%) (Figure 3f). The salt gradually and selectively crystallized on the side thread that contacted the superhydrophobic sponge@MPN-OTS rather than the top surface or inside of the evaporator (Figure 3f; Figure S20–S24, Supporting Information). The directional salt crystallization enabled sufficient space on the side surfaces of the evaporator for vapor escape and therefore maintained the high and stable water evaporation rate over a long period (i.e., 10 h). In contrast, Evap-5, composed of superhydrophilic sponges only, was completely covered with salt crystals, leading to a severe decrease in the water evaporation rate (Figure 3g).

Evap-1 also exhibited outstanding performance in treating actual concentrated seawater (20 wt%). It is notable that natural seawater also contains other metal species (e.g., magnesium), which typically do not receive considerable attention in this field but may cause significant effects (e.g., reducing the water evaporation rate to zero) in actual industrial desalination.[34] As observed from Figure 3h, the water evaporation rate of Evap-1 remained >2 kg m^{-2} h^{-1} under one sun illumination without the need for additional salt crystallization inhibitor or additives. Evap-1 demonstrated a long-term and stable desalination rate of ≈2.1–2.6 kg m^{-2} h^{-1} for highly concentrated seawater for up to 21 days without significant decrease in the selective wettability of the MPN-engineered sponges (Figure S25 and Movies S3 and S4, Supporting Information). Note that directional salt crystallization on the thread of the evaporator was also observed, and these salt crystals could be easily peeled off and recycled. Considering that salts are crystallized and recycled as a solid by-product, using the current technology, no highly concentrated brine waste would be discharged to water bodies and cause environmental consequences.

The mechanism of the directional crystallization operating within the 3D evaporator was studied. Salt crystallization on the thread mainly occurs on the segments that contact the superhydrophobic sponges (**Figure 4**a; Figure S26, Supporting Information). As shown in Figure 4b, the temperature of sponge@MPN-OTS (≈35 °C) is higher than the adjacent sponge@MPN (≈31 °C), leading to the relatively higher temperature of the thread contacting the surface of sponge@MPN-OTS than that of sponge@MPN (Figure 4d; Figure S27, Supporting Information). The higher temperature leads to rapid water evaporation, and the remaining brine becomes more concentrated and precipitates readily (Figure 4d). Moreover, the thread attached to the sponge@MPN can exchange and pump water from the superhydrophilic sponge (Figure 4c). A limited volume of brine then flows into the thread that contacts sponge@MPN-OTS at a low speed of 0.5 mm s^{-1} (Figure 4c; Figure S28 and S29, Supporting Information). These results collectively suggest that the brine in the thread that contacts sponge@MPN-OTS reaches saturation point first and generates salt crystals on the thread, leading to directional salt crystallization (Figure 4d).

2.4. Outdoor Solar Desalination and Directional Salt Crystallization

An upscale model of Evap-1 was constructed for the outdoor solar desalination studies, which involved condensing the generated water vapor and collecting the clean water (**Figure 5**a; Figure S30, Supporting Information). The device operated outdoors under natural sun irradiation for 8 h (from 9:00 to 17:00). Direct salt crystallization was observed when treating seawater with different concentrations (Figure 5b; Figure S31 and S32,

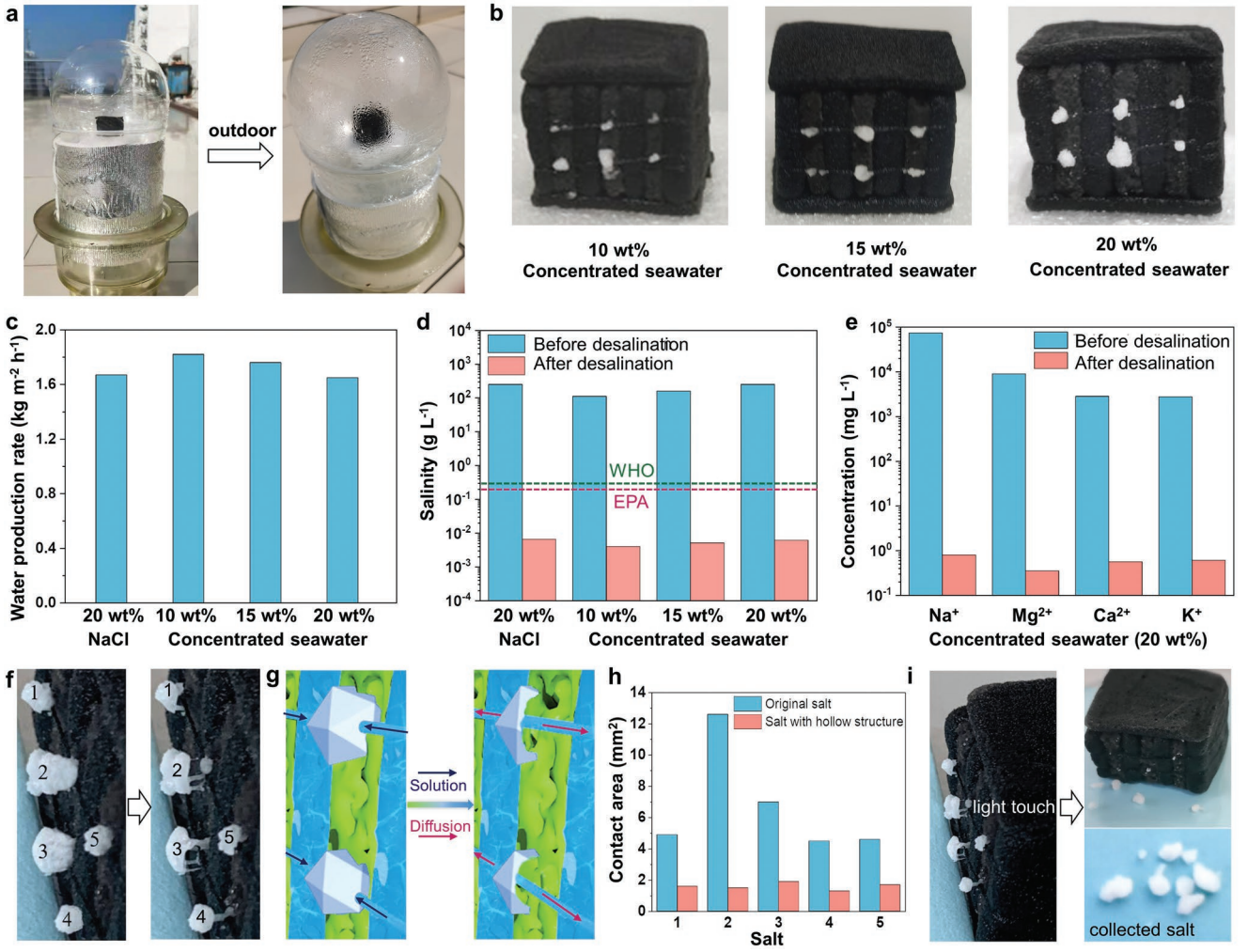

Figure 5. a) Photographs of the upscale evaporator device based on Evap-1 before (left) and after (right) outdoor seawater desalination. b) Photographs of 3D evaporators depicting the occurrence of directional salt crystallization after treating concentrated seawater for 8 h outdoor. c) Water production rate of the upscale evaporator device upon treatment of salt brine. d) Salinity of treated water from different sources before and after desalination. The salinity of drinking water standards set by WHO and EPA is also shown for comparison. e) Concentration of different metal ions before and after desalination of 20 wt% concentrated seawater. f) Photographs of salt crystals evolving from a non-hollow (left) to a hollow (right) structure after sunlight irradiation is ceased. g) Schematic of the formation of the hollow salt crystals via a solution-diffusion process. h) Contact areas between non-hollow or hollow salt crystals and surface of different evaporators. i) Photographs of salt that can be easily removed by light mechanical agitation and which can be subsequently recycled.

Supporting Information). The water production rates of the upscale evaporator were ≈1.67, 1.82, 1.76, and 1.65 kg m^{-2} h^{-1} for the treatment of 20 wt% NaCl, and 10, 15, and 20 wt% concentrated seawater, respectively. The salinity of the obtained water decreased by about four orders of magnitude (from above 100 g L^{-1} to below 0.01 g L^{-1}) (Figure 5d), which surpasses the drinking water standards set by the World Health Organization (WHO) and Environmental Protection Agency (EPA).[39] The concentrations of Na^+, Mg^{2+}, Ca^{2+}, and K^+ were also significantly reduced by three-to-four orders of magnitude after solar desalination (Figure 5e; Figure S33, Supporting Information). Interestingly, the salt crystals formed a hollow structure with two spindly "legs" 30 min after sunlight irradiation was ceased (Figure 5f). We speculate that the evaporation rate of water on the thread is reduced considerably in the absence of solar irradiation, while water is still continuously pumping into threads from sponge@MPN, which partially dissolves the salt, resulting in a hollow structure (Figure 5g,h). Of particular interest, the resultant salt crystals can be easily removed and recycled from the evaporator via gentle shaking (Figure 5i; Movie S5, Supporting Information).

3. Conclusion

We have designed a 3D evaporator via materials design and structural engineering to achieve sustained and highly efficient desalination for high-salinity brine. Melamine sponges were modified with MPNs to achieve photothermal effects and selective wettability; the superhydrophilic and superhydrophobic features formed the basis of the water-pumping channels and gas escape channels, respectively, generated within the 3D evaporators. The modified sponges

were then assembled into 3D evaporators, involving the alternate arrangement of the sponges secured with hydrophilic nylon threads. Salts selectively crystallized on the side-twining threads that contacted the superhydrophobic photothermal sponges, thus avoiding salt accumulation on the top surface of the evaporator and achieving zero liquid discharge. In the presence of 20 wt% seawater, the 3D evaporator exhibited a high and stable evaporation rate (average ≈2.3 kg m^{-2} h^{-1}) under 1 sun irradiation over 21 days. During the outdoor operation process, the device also exhibited outstanding directional salt crystallization and clean water production rate (1.65–1.82 kg m^{-2} h^{-1}) when treating different concentrated brine (i.e., 10, 15, and 20 wt% seawater). This work is expected to advance fundamental and applied research in metal–organic materials and solar evaporators for high-salinity brine from materials design and structural engineering perspectives.

Supporting Information

Supporting Information is available from the Wiley Online Library or from the author.

Acknowledgements

This work was supported by the National Natural Science Foundation of China (Nos. 22279050 and 51903115), the Jiangxi Province Natural Science Foundation (20212ACB214013), and the Australian Research Council Discovery Project (DP200100713).

Open access publishing facilitated by The University of Melbourne, as part of the Wiley - The University of Melbourne agreement via the Council of Australian University Librarians.

Conflict of Interest

The authors declare no conflict of interest.

Data Availability Statement

The data that support the findings of this study are available from the corresponding author upon reasonable request.

Keywords

directional crystallization, metal–organic materials, polyphenols, selective wettability, solar desalination

Received: September 30, 2022
Published online: December 8, 2022

[1] C. J. Vorosmarty, P. Green, J. Salisbury, R. B. Lammers, *Science* **2000**, *289*, 284.
[2] P. J. Alvarez, C. K. Chan, M. Elimelech, N. J. Halas, D. Villagrán, *Nat. Nanotechnol.* **2018**, *13*, 634.
[3] N. Hanikel, M. S. Prévot, O. M. Yaghi, *Nat. Nanotechnol.* **2020**, *15*, 348.
[4] M. M. Mekonnen, A. Y. Hoekstra, *Sci. Adv.* **2016**, *2*, e1500323.
[5] H. B. Park, J. Kamcev, L. M. Robeson, M. Elimelech, B. D. Freeman, *Science* **2017**, *356*, eaab0530.
[6] A. V. Dudchenko, C. Chen, A. Cardenas, J. Rolf, D. Jassby, *Nat. Nanotechnol.* **2017**, *12*, 557.
[7] T. Liu, M. S. Mauter, *Joule* **2022**, *6*, 1199.
[8] M. Elimelech, W. A. Phillip, *Science* **2011**, *333*, 712.
[9] D. A. Roberts, E. L. Johnston, N. A. Knott, *Water Res.* **2010**, *44*, 5117.
[10] P. Tao, G. Ni, C. Song, W. Shang, J. Wu, J. Zhu, G. Chen, T. Deng, *Nat. Energy* **2018**, *3*, 1031.
[11] F. Zhao, X. Zhou, Y. Shi, X. Qian, M. Alexander, X. Zhao, S. Mendez, R. Yang, L. Qu, G. Yu, *Nat. Nanotechnol.* **2018**, *13*, 489.
[12] M. Gao, L. Zhu, C. K. Peh, G. W. Ho, *Energy Environ. Sci.* **2019**, *12*, 841.
[13] M. Zou, Y. Zhang, Z. Cai, C. Li, Z. Sun, C. Yu, Z. Dong, L. Wu, Y. Song, *Adv. Mater.* **2021**, *33*, 2102443.
[14] E. Chiavazzo, M. Morciano, F. Viglino, M. Fasano, P. Asinari, *Nat. Sustainability* **2018**, *1*, 763.
[15] H. Li, W. Zhu, M. Li, Y. Li, R. T. K. Kwok, J. W. Y. Lam, L. Wang, D. Wang, B. Z. Tang, *Adv. Mater.* **2021**, *33*, 2102258.
[16] S. C. Singh, M. ElKabbash, Z. Li, X. Li, B. Regmi, M. Madsen, S. A. Jalil, Z. Zhan, J. Zhang, C. Guo, *Nat. Sustainability* **2020**, *3*, 938.
[17] K. Xu, C. Wang, Z. Li, S. Wu, J. Wang, *Adv. Funct. Mater.* **2020**, *31*, 2007855.
[18] N. Xu, J. Li, Y. Wang, C. Fang, X. Li, Y. Wang, L. Zhou, B. Zhu, Z. Wu, S. Zhu, J. Zhu, *Sci. Adv.* **2019**, *5*, eaaw7013.
[19] F. Zhao, Y. Guo, X. Zhou, W. Shi, G. Yu, *Nat. Rev. Mater.* **2020**, *5*, 388.
[20] D. Jassby, T. Y. Cath, H. Buisson, *Nat. Nanotechnol.* **2018**, *13*, 670.
[21] W. Xu, X. Hu, S. Zhuang, Y. Wang, X. Li, L. Zhou, S. Zhu, J. Zhu, *Adv. Energy Mater.* **2018**, *8*, 1702884.
[22] J. Wang, Y. Chen, Q. Xu, M. Cai, Q. Shi, J. Gao, *Sci. Rep.* **2021**, *11*, 11960.
[23] S. Wu, Y. Du, Y. Alsaid, D. Wu, M. Hua, Y. Yan, B. Yao, Y. Ma, X. Zhu, X. He, *Proc. Natl. Acad. Sci. USA* **2020**, *117*, 11240.
[24] L. Zhou, Y. Tan, J. Wang, W. Xu, Y. Yuan, W. Cai, S. Zhu, J. Zhu, *Nat. Photonics* **2016**, *10*, 393.
[25] H. Ejima, J. J. Richardson, K. Liang, J. P. Best, M. P. van Koeverden, G. K. Such, J. Cui, F. Caruso, *Science* **2013**, *341*, 154.
[26] J. Guo, B. L. Tardy, A. J. Christofferson, Y. Dai, J. J. Richardson, W. Zhu, M. Hu, Y. Ju, J. Cui, R. R. Dagastine, *Nat. Nanotechnol.* **2016**, *11*, 1105.
[27] J. Zhou, Z. Lin, Y. Ju, M. A. Rahim, J. J. Richardson, F. Caruso, *Acc. Chem. Res.* **2020**, *53*, 1269.
[28] Z. Lin, J. Zhou, C. Cortez-Jugo, Y. Han, Y. Ma, S. Pan, E. Hanssen, J. J. Richardson, F. Caruso, *J. Am. Chem. Soc.* **2020**, *142*, 335.
[29] H. Geng, Q.-Z. Zhong, J. Li, Z. Lin, J. Cui, F. Caruso, J. Hao, *Chem. Rev.* **2022**, *122*, 11432.
[30] Z. Wang, H.-C. Yang, F. He, S. Peng, Y. Li, L. Shao, S. B. Darling, *Matter* **2019**, *1*, 115.
[31] S. Pan, J. J. Richardson, A. J. Christofferson, Q. A. Besford, T. Zheng, B. J. Wood, X. Duan, M. J. Jara Fornerod, C. F. McConville, I. Yarovsky, S. Guldin, L. Jiang, F. Caruso, *J. Am. Chem. Soc.* **2021**, *143*, 9972.
[32] Z. Lin, J. Zhou, Y. Qu, S. Pan, Y. Han, R. P. M. Lafleur, J. Chen, C. Cortez-Jugo, J. J. Richardson, F. Caruso, *Angew. Chem., Int. Ed.* **2021**, *60*, 24968.
[33] A. K. Menon, I. Haechler, S. Kaur, S. Lubner, R. S. Prasher, *Nat. Sustainability* **2020**, *3*, 144.
[34] C. Zhang, Y. Shi, L. Shi, H. Li, R. Li, S. Hong, S. Zhuo, T. Zhang, P. Wang, *Nat. Commun.* **2021**, *12*, 998.
[35] Z. Wang, X. Wu, F. He, S. Peng, Y. Li, *Adv. Funct. Mater.* **2021**, *31*, 2011114.
[36] T. Liu, M. Zhang, W. Liu, X. Zeng, X. Song, X. Yang, X. Zhang, J. Feng, *ACS Nano* **2018**, *12*, 3917.
[37] Y. Wang, X. Sun, S. Tao, *Environ. Sci. Technol.* **2020**, *54*, 16240.
[38] Z. Xu, L. Zhang, L. Zhao, B. Li, B. Bhatia, C. Wang, K. L. Wilke, Y. Song, O. Labban, J. H. Lienhard, R. Wang, E. N. Wang, *Energy Environ. Sci.* **2020**, *13*, 830.
[39] W. H. Organization, Safe Drinking-Water from Desalination, http://apps.who.int/iris/bitstream/handle/10665/70621/WHO%20HSE%20WSH%2011.%2003%20eng.pdf?sequence=1 (accessed: July 2022).